MALAYSIAN JOURNAL OF MICROSCOPY

Journal homepage: https://malaysianjournalofmicroscopy.org

RESEARCH ARTICLE

PHASE STABILITY AND OXIDATION MECHANISM DIVERGENCE IN $Al_{30}Cr_{15}Ni_{15}Si_{10}Ti_{30}$ HIGH-ENTROPY ALLOY AT 1000 °C

Mudassar Hussain[1, 2], Junsen Wang[2], Abdillah Sani Mohd Najib[1], Nor Akmal Fadil[1], Jing Liu[2], and Tuty Asma Abu Bakar[1, 3,*]

[1]Materials Research and Consultancy Group (MRCG), Department of Materials, Manufacturing & Industrial Engineering, Faculty of Mechanical Engineering, Universiti Teknologi Malaysia, 81310 Johor Bahru, Johor, Malaysia.
[2]Guangdong Provincial Key Laboratory of New Energy Materials Service Safety, College of Materials Science and Engineering, Shenzhen University, Shenzhen, Guangdong, P.R. China.
[3]Centre of Advanced Composite Materials, Universiti Teknologi Malaysia,81310 Johor Bahru, Johor, Malaysia.

Abstract. AlCrNiSiTi high-entropy alloys (HEAs) are promising candidates as next-generation competitors to Ni-based superalloys and refractory alloys, offering low density and notable phase stability for high-temperature applications. However, their oxidation performance at elevated temperatures showed limitations due to complex oxidation behaviour. This study investigates the phase stability and oxidation response of an as-cast $Al_{30}Cr_{15}Ni_{15}Si_{10}Ti_{30}$ HEA at 1000 °C for 100 hours. A systematic characterisation and performance evaluation framework is adopted, encompassing X-ray diffraction (XRD), scanning electron microscopy with energy-dispersive spectroscopy (SEM-EDS), electron probe microanalysis (EPMA), X-ray photoelectron spectroscopy (XPS), and differential scanning calorimetry (DSC). Structural and elemental investigations revealed the formation of nonprotective multielement oxides. The oxide scale is dominated by rapid, extensive TiO_2 formation, resulting in a porous, poorly adherent surface layer. Beneath this, a discontinuous Al_2O_3 sublayer forms with dispersed $(NiCr)_2O_3$ and SiO_2, but it fails to develop into a continuous protective scale. As a result, the alloy exhibits a relatively high total mass gain of 2.1 mg cm^{-2}, significantly higher than alloys capable of forming a continuous Al_2O_3 barrier (<1 mg cm^{-2} under similar conditions). Oxidation kinetics exhibit a clear three-stage parabolic behaviour, with rate constants of $k_{p1} = 4.5 \times 10^{-2}$, $k_{p2} = 2.6 \times 10^{-2}$, and $k_{p3} = 1.9 \times 10^{-2}$ mg^2 cm^{-4} h^{-1} for the early, intermediate, and late stages, respectively. A global parabolic rate constant of $k_p = 3.14 \times 10^{-2}$ mg^2 cm^{-4} h^{-1} reflects the overall diffusion-controlled oxidation process. However, DSC analysis up to 1400 °C confirms the absence of solid-state phase transformations, aside from the melting peaks of individual phases, thereby identifying the melting range of the alloy. The findings highlight pronounced phase stability but limited oxidation resistance, emphasising the need for compositional tuning for extreme-temperature applications.

Keywords: Al-Ti-rich AlCrNiSiTi high-entropy alloy, phase stability, high-temperature oxidation, TiO_2 formation, limited oxidation resistance.

Article Info

Received 8 January 2026
Accepted 11 May 2026
Published 8 June 2026

***Corresponding author: tuty@utm.my**

ISSN: 1823-7010, eISSN: 2600-7444

1. INTRODUCTION

The continuous demand for structural materials that withstand progressively higher temperatures while delivering improved specific strength and reduced mass has driven intense research into alternatives to conventional Ni-based superalloys and traditional refractory alloys [1-4]. The deployment of conventional Ni-based superalloys in extreme thermal environments is fundamentally constrained by an inescapable trade-off between mechanical performance and surface stability. At operating temperatures approaching 720 °C and beyond, these alloys suffer from the rapid phase dissociation of critical strengthening precipitates (γ'' → γ'), leading to catastrophic loss of strength, while the protective Cr_2O_3 scale undergoes transformation to volatile CrO at 900 °C, resulting in its sublimation and leaving the substrate vulnerable to accelerated oxidation [5,6]. Compounding these issues is the inherent high density of Ni-alloys, which diminishes the specific strength and efficiency in aerospace and power generation applications [7]. To bridge this technological gap, the AlCrNiSiTi high-entropy alloy system emerges as a rationally designed candidate, moving beyond single-principal-element design. This system strategically leverages a high configurational entropy to potentially stabilize a robust microstructure against thermal dissociation, while the synergistic combination of Al and Cr is intended to form a tenacious, slow-growing Al_2O_3 scale, thereby overcoming the limitations of transient chromia. Furthermore, the incorporation of lightweight elements like Al and Ti directly addresses the density penalty of traditional superalloys, offering a pathway to develop next-generation materials that concurrently fulfil the demanding criteria of phase stability, oxidation resistance, and specific strength for ultra-high-temperature service [8]. Refractory alloys can provide superior high-temperature strength but commonly suffer from ambient-temperature brittleness and limited oxidation resistance, constraining their broad adoption in aerospace and power-generation applications [9].

HEAs depart from classical alloy design by employing multiple principal elements (typically five or more) in near-equiatomic ratios. This design strategy invokes several often-cited core effects: high configurational entropy, severe lattice distortion, sluggish diffusion, and the so-called cocktail effect, which together can stabilise simple solid-solution phases, hinder deleterious phase transformations, and produce emergent mechanical and chemical behaviours not accessible in conventional alloys [10]. These features are particularly attractive for high-temperature applications: high configurational entropy and sluggish diffusion can suppress precipitation and coarsening, while severe lattice distortion contributes to solid-solution strengthening and elevated creep resistance in certain compositions. Recent comprehensive reviews summarise these advantages and highlight the promise of HEAs for structural, corrosion-resistant, and oxidation-resistant applications at elevated temperatures [11].

Despite their theoretical appeal, realising practical high-temperature HEAs requires careful control of composition and microstructure. Lightweight constituents such as Al and Ti are attractive for reducing density and enhancing specific strength, but they also introduce competing oxidation behaviours. Al is well known to form the protective, slow-growing Al_2O_3 scale under appropriate conditions, thereby conferring excellent oxidation resistance in many alumina-forming alloys [12]. Ti, however, preferentially forms TiO_2 under oxidising conditions; TiO_2 tends to be porous and poorly adherent compared to Al_2O_3, enabling sustained oxygen ingress and internal oxidation [13]. Cr contributes to oxidation resistance by forming Cr_2O_3, which can be protective under certain regimes, and Ni is typically employed to stabilise ductile phases and improve high-temperature mechanical behaviour [14]. Si is often added in small amounts to promote glassy or silica-containing sublayers that impede oxygen transport and improve scale adherence [15]. The interplay of these elements in multi-principal-element alloys results in complex, composition-dependent oxidation pathways that can either promote protective scale formation or, conversely, lead to non-protective mixed-oxide layers.

Because of these competing tendencies, Al-Ti-rich HEAs occupy a promising but challenging design space. Studies on Al–Ti-containing HEAs show that appropriate balances of Al, Ti, and Cr can yield alloys that form continuous alumina- or chromia-rich scales and therefore exhibit improved oxidation resistance at elevated temperatures. However, when Ti content is high relative to Al and Cr, oxidation often becomes dominated by TiO_2 formation, producing porous, non-adherent scales that

compromise long-term oxidation resistance. Numerical and experimental works investigating TiO_2 and Al_2O_3 scale growth establish that preferential oxidation of Ti can kinetically inhibit the outward transport of Al and Cr required to nucleate and sustain continuous Al_2O_3 or Cr_2O_3 layers, a phenomenon often referred to as oxidation mechanism divergence [16,17].

Recent experimental investigations demonstrate the nuanced outcomes of compositional tuning. For example, Al additions to certain refractory HEAs have been shown to improve oxidation resistance by promoting Al_2O_3 formation and suppressing pestering, but the threshold Al content and the coexisting presence of Ti or other strong oxygen-affinity elements critically determine whether a protective scale forms or whether non-protective mixed oxides dominate [15,18,19]. Similarly, targeted alloying and microstructural control, such as introducing Si or optimising Cr content, can help form silica- or chromia-enriched sublayers that retard oxygen transport and stabilise protective alumina/chromia scales.

Several investigations into high-temperature oxidation of HEAs at 800-1100 °C have reported divergent behaviour depending on elemental makeup. Refractory HEAs frequently demonstrate parabolic oxidation kinetics and dense oxide scales when Al content and diffusion pathways favour continuous alumina formation; in contrast, Al–Ti-rich compositions with insufficient Al/Cr activity tend to form TiO_2-dominated scales with accelerated mass gain and poor adherence [20-23]. Recent high-quality studies analysing oxide scale chemistry with X-ray photoelectron spectroscopy (XPS), scanning electron microscopy (SEM-EDS), and thermogravimetric analysis (TGA) have elucidated how initial rapid Ti oxidation forms an outer TiO_2 layer that blocks Al/Cr outward diffusion, resulting in internal oxidation of Al and the development of porous internal oxide regions. These microstructural signatures correlate strongly with increased mass gain, scale porosity, and a lack of protective behaviour when compared to alloys that sustain continuous Al_2O_3 or Cr_2O_3 scale growth.

Within this broader context, the $Al_{30}Cr_{15}Ni_{15}Si_{10}Ti_{30}$ composition represents a targeted design that intentionally emphasises Al and Ti to achieve lightweight and specific-strength objectives, while retaining moderate Cr and Ni to support stability and oxidation resistance, and a modest Si content to potentially improve scale compactness. However, while such a composition benefits from high configurational entropy and potential B_2/BCC ordering, which is favourable for phase stability, the high Ti fraction raises the spectre of Ti-driven oxidation pathways that could undermine surface protection. To date, systematic studies that couple robust phase-stability assessment (e.g., DSC and high-temperature XRD) with long-duration oxidation testing (e.g., 100 h at 1000 °C) and modern surface-chemical analysis (XPS) for this Al-Ti-rich AlCrNiSiTi system are limited. RHEAs exhibit thick, continuous oxidation, better phase stability, and high bulk density, whereas Ni-based superalloys demonstrate notable oxidation resistance at the expense of Al-rich phase dissolution, compromising phase stability.

This study aims to reveal the fundamental conflict between phase stability and oxidation resistance in high-Ti containing $Al_{30}Cr_{15}Ni_{15}Si_{10}Ti_{30}$ HEA by combining phase-stability characterization and detailed oxidation-scaling analysis. Specifically, we (1) evaluate the phase stability of as-cast $Al_{30}Cr_{15}Ni_{15}Si_{10}Ti_{30}$ up to 1400 °C using DSC and XRD to confirm whether the bulk microstructure remains stable under extreme thermal exposure; (2) quantify oxidation kinetics at 1000 °C using weight gain method over 100 hours to capture both initial transient behaviour and longer-term kinetics; (3) elucidate oxide-scale morphology, adherence, and chemical states via SEM-EDS, EPMA, and XPS; and (4) correlate oxide-forming tendencies with elemental activities and diffusion pathways to explain the suppression of protective Al_2O_3/Cr_2O_3 formation in favour of TiO_2 dominated scales, if observed. By integrating phase and surface analyses, we aim to clarify the intrinsic causes of oxidation mechanism divergence in Al-Ti-rich HEAs and to provide practical recommendations—composition tuning—for achieving balanced high-temperature performance.

2. MATERIALS AND METHODS

2.1 Alloy Synthesis

An alloy with a nominal composition of $Al_{30}Cr_{15}Ni_{15}Si_{10}Ti_{30}$ (at.%) was prepared by arc-melting a mixture of high-purity metals (>99.9 wt.%) in a water-cooled copper hearth under a high-purity argon atmosphere at Yuanshun Advanced Materials Co. Ltd, Zhuhai, China. To ensure chemical homogeneity, the ingot was flipped and re-melted at least five times, and chemical composition was analysed by ICP-OES to confirm homogeneity. The resulting button-shaped ingot, approximately 50 g in weight, was used in the as-cast condition for all subsequent experiments.

2.2 Phase Stability Analysis

The thermal stability of the as-cast alloy was investigated using standardised Differential Scanning Calorimetry (DSC, Netzsch STA 449 F3). A sample of ~30 mg was heated in an alumina crucible from 50 °C to 1400 °C at a constant rate of 20 °C/min under a flowing argon atmosphere.

2.3 High-Temperature Oxidation Testing

Isothermal oxidation tests were conducted in a static air atmosphere without continuous flow to air at 1000 °C for 100 hours using an electric heating furnace and were weighed at regular intervals of 10 hours. Two samples were drawn at each internal and the weight gain was averaged to ensure statistical correctness and experimental repeatability. Rectangular coupons (approx. 10 mm x 5 mm x 2 mm) were ground to a 1100-grit SiC finish, ultrasonically cleaned in acetone and ethanol, and dried before loading for weight gain test and change was continuously recorded with a sensitivity of ±1 μg.

2.4 Microstructural and Chemical Characterization

The phase constitution of the as-cast and oxidized samples was identified by XRD (Rigaku Miniflex600) with Cu Kα radiation (λ = 1.5406 Å) over a 2θ range of 20 ° to 120 ° at a step size of 0.02° and a scanning speed of 10°/min. The microstructure and surface chemical composition of the samples were characterized using SEM (Hitachi SU-70 SEM) equipped with an EDS system. Cross-sectional samples of the oxidized coupons were prepared by standard metallographic techniques and analysed for elemental distribution using EPMA-1720HT. The chemical states of elements in the oxide scale were analysed by XPS (Thermo-Scientific K-Alpha+) with a monochromatic Al Kα X-ray source was performed by alternating Ar^+ ion sputtering and XPS analysis.

3. RESULTS AND DISCUSSION

3.1 As-Cast vs Oxidised Microstructure and Phase Identification

Figure **1** shows SEM-EDS analysis, where the Ti and Si rich region represents Ti_5Si_4 while Al and Ni rich areas present AlNi phase and rest of the area fraction is rich in Cr, Ti and Si. This partitioning behaviour reflects the competing affinities among the elements: the high negative mixing enthalpy between Ti and Si drives their co-segregation, yet the overall stoichiometry limits excessive growth into coarse intermetallics. The relatively uniform distribution of Al and Ni supports stabilisation of a continuous BCC/B2-type matrix.

The as-cast $Al_{30}Cr_{15}Ni_{15}Si_{10}Ti_{30}$ alloy exhibits a multi-phase microstructure, as annotated on backscattered electron (BSE) imaging (

Figure **2**(a)). This chemical inhomogeneity is typical of high-entropy alloys with elements that have large electronegativity differences, such as Ti-Si and Al-Ni. The concentrations of strong oxide-forming elements like Al and Ti pre-defines the competing oxidation behaviour observed, as different

phases will possess varying susceptibilities to oxidation. Following oxidation at 1000 °C, the surface topography undergoes a dramatic transformation.

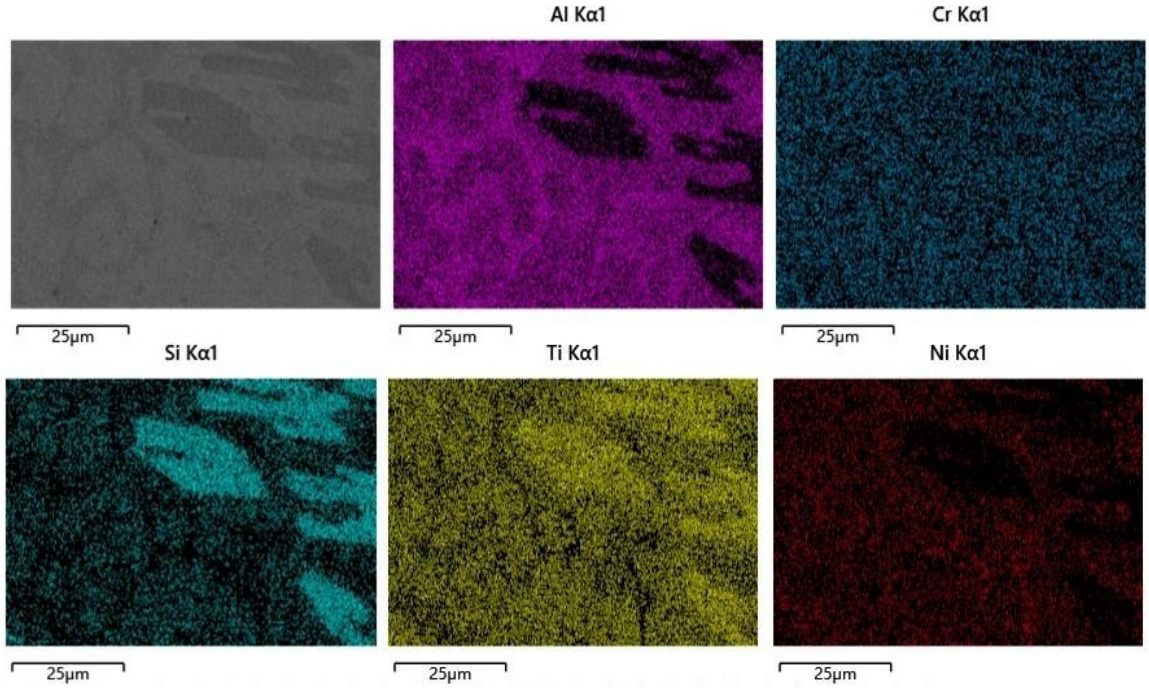

Figure 1: SEM-EDS elemental maps of the as-cast $Al_{30}Cr_{15}Ni_{15}Si_{10}Ti_{30}$ high-entropy alloy

The dominant feature is porous and discontinuous, indicative of a non-protective oxide predominantly TiO_2. Embedded within this matrix are nodular (Al_2O_3) and whisker-like features (TiO_2), suggesting the outward diffusion of cations and the subsequent nucleation of oxides such as $(Ni,Cr)_2O_3$ spinel (

Figure **2**(b)). The overall lack of dense, continuous surface morphology is the first visual indicator of the alloy's compromised oxidation resistance. This is consistent with the rapid growth of TiO_2, which is known to form a non-adherent, non-protective rutile scale at high temperatures in Ti rich high entropy alloys [16]. However, in the as-cast condition, the contrast variations indicate significant elemental segregation, with the presence of at least three distinct phases (Ti_5Si_4, $Cr_{2.2}Ti_{0.8}Si$, and AlNi) as identified by the black XRD pattern of the as-cast sample (

Figure **2**(c)). The XRD pattern (

Figure **2**(c)) from the oxidised surface (red) provides definitive phase identification, confirming the multi-phase nature of the oxide scale. The dominant peaks correspond to TiO_2, affirming its role as the primary oxidation product. Clear peaks for a $(Ni,Cr)_2O_3$ spinel are also present, corroborating the nodular features observed in the topography. The presence of Al_2O_3 confirms that a protective alumina layer forms, but its relatively lower peak intensity compared to TiO_2 suggests it exists as an internal layer beneath the Ti-rich outer scale, rather than as a continuous external layer. The detection of SiO_2 indicates silicon's participation in the oxidation process, though it does not form a continuous film. Crucially, the persistence of base material peaks, specifically Ti_5Si_4, $Cr_{2.2}Ti_{0.8}Si$, and AlNi, in the oxidised sample is highly significant. This indicates that the subsurface zone has been enriched with these phases indicating depth sensitivity of the XRD technique and identifying the underlying matrix microstructure.

The collective data reveals a coherent oxidation narrative. The as-cast multiphase structure provides numerous pathways for rapid, selective oxidation. The resulting oxide scale is stratified: a non-protective outer layer of TiO_2 and $(Ni,Cr)_2O_3$ spinel, underlain by a protective but internally formed layer of Al_2O_3. The XRD results directly confirm this phase assemblage. The formation of an internal Al_2O_3 layer, rather than an external one, is the key factor that moderates but does not eliminate poor

oxidation resistance. This failure to form an exclusive external alumina scale is directly attributable to the high Ti content, which dominates the initial oxidation kinetics [17].

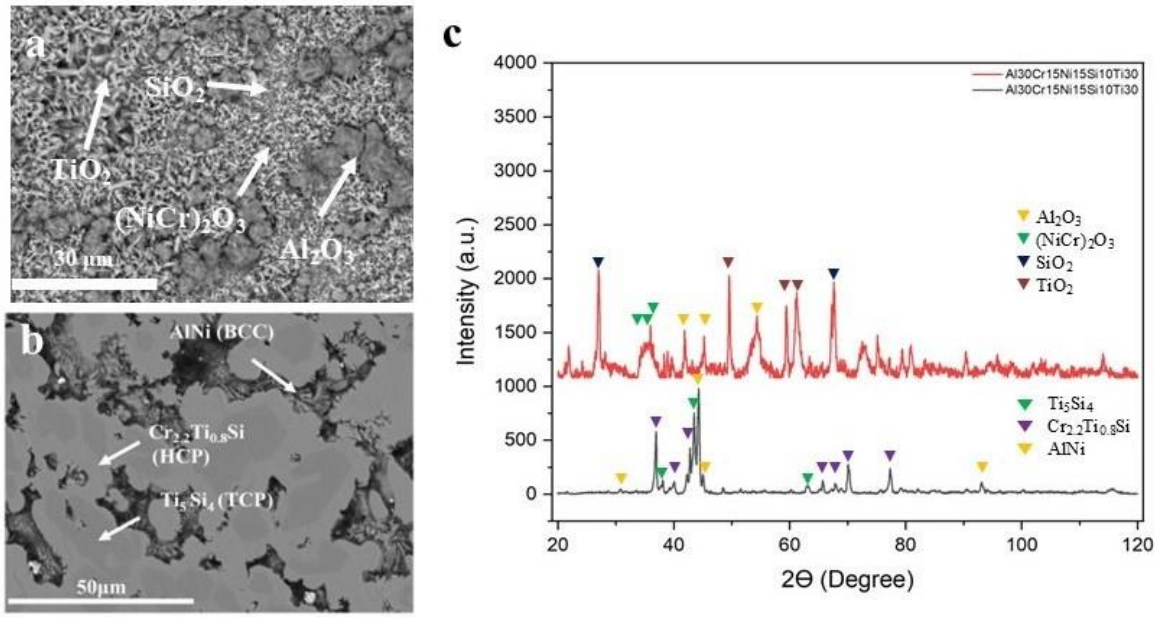

Figure 2: (a) Oxide-scale morphology of $Al_{30}Cr_{15}Ni_{15}Si_{10}Ti_{30}$ after oxidation at 1000 °C, showing TiO_2, $(Ni,Cr)_2O_3$, SiO_2, and Al_2O_3, (b) As-cast microstructure containing AlNi, $Cr_{2.2}Ti_{0.8}Si$, and Ti_5Si_4, and (c) XRD patterns of as-cast and oxidized states confirming the formation of mixed oxides after high-temperature exposure

3.2 Assessment of Phase Stability

Figure **3** shows differential scanning calorimetry (DSC) results of the $Al_{30}Cr_{15}Ni_{15}Si_{10}Ti_{30}$ high-entropy alloy, revealing excellent thermal stability from room temperature up to approximately 1100 °C, as evidenced by a nearly straight baseline with no detectable phase transformations or thermal events. A minor endothermic hump observed between 50-150 °C is attributed to the desorption of adsorbed moisture and volatiles, which is a common instrumental artifact and holds no structural significance for the alloy. Significant thermal events occurred only in the high-temperature regime. The magnified inset and shaded region clearly resolved three distinct endothermic peaks between 1150-1300 °C, indicating a broad melting range of approximately 150 °C. The first endothermic peak (onset ~1180 °C) corresponds to the solidus temperature, associated with the initial melting of the lower-melting Al-Ni-rich phase. The second, sharper peak (~1200 °C) represents intermediate melting of another phase, probably the Cr-Ti-Si-rich phase and the third largest peak (~1280 °C) is the liquidus temperature, marking the complete melting of the probably higher-melting Ti–Si-rich phase. This multi-stage melting behaviour is characteristic of multi-principal-element alloys, where different constituent phases melt sequentially rather than congruently. The observed melting range is consistent with the multi-phase microstructure identified by SEM-EDS, comprising Al-Ni-rich, Cr-Ti-Si-rich, and Ti–Si-rich regions [20]. These findings imply that the alloy maintains structural integrity up to ~1100 °C but cannot be used in service above this temperature without risk of partial melting. The results provide critical guidance for melting, casting, and high-temperature application limits of this Al-Ti-rich high-entropy alloy.

The notable phase stability of the as-cast $Al_{30}Cr_{15}Ni_{15}Si_{10}Ti_{30}$ high-entropy alloy (HEA) up to 1100 °C is closely linked to its intrinsic high-entropy stabilisation effect and synergistic thermodynamic balance among constituent elements. Moreover, the differential scanning calorimetry (DSC) data confirmed the absence of endothermic/exothermic events up to 1100 °C, implying no ordering–

disordering transformations or solid-state decomposition. Such thermal robustness has also been observed in AlCrFeNiTi HEAs, where the strong covalent Al-Ti bonding contributes to enhanced lattice cohesion [24]. The addition of Si likely further stabilises the microstructure through solid-solution strengthening and reduced atomic diffusion rates, as demonstrated in Si-containing HEAs [25]. Hence, the stability observed in this study stems from a delicate interplay of configurational entropy, strong Al–Ti bonding, and kinetic sluggishness, the "core effects" that define HEAs.

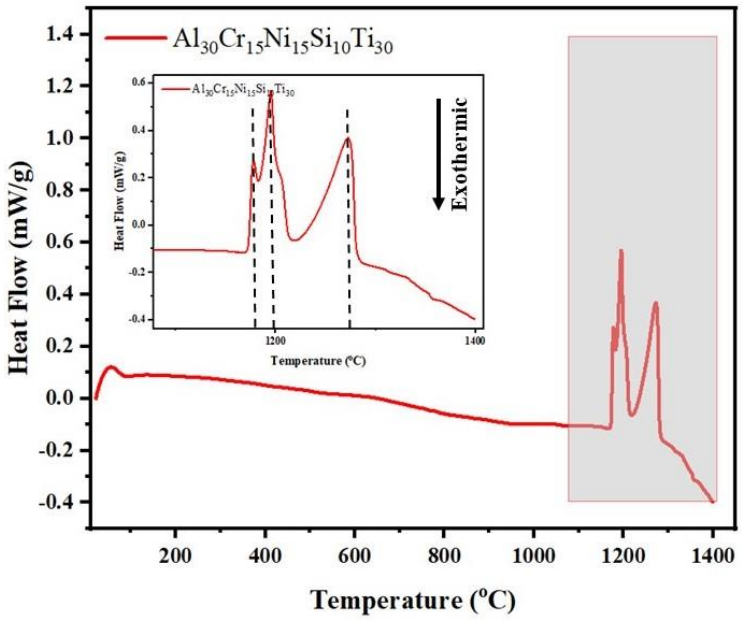

Figure 3: DSC heating curve of the $Al_{30}Cr_{15}Ni_{15}Si_{10}Ti_{30}$ alloy, showing low-temperature relaxation and multiple high-temperature endothermic peaks (1150-1300 °C) associated with individual phase melting

3.3 Oxidation Kinetics

Figure **4**(a) shows the isothermal oxidation curve of the $Al_{30}Cr_{15}Ni_{15}Si_{10}Ti_{30}$ high-entropy alloy exposed at 1000 °C for 100 h in ambient air. The weight gain increases smoothly from zero to 2.16 mg cm^{-2}, with no evidence of breakaway oxidation throughout the exposure period. The overall oxidation behaviour follows a parabolic growth law, confirmed by the linear dependence of $(\Delta W)^2$ as indicated in equation (1) on time, as shown in
Figure **4**(b).

$$(\Delta W)^2 = k_p t + C \tag{1}$$

yielding:

$$k_p = 3.14 \times 10^{-2}\ \text{mg}^2\ \text{cm}^{-4}\ \text{h}^{-1} \tag{2}$$

The dominance of parabolic kinetics indicates that the alloy forms a protective, diffusion-controlled oxide scale, consistent with that reported for Al-rich HEAs in the literature [26]. Although the overall kinetics are parabolic, the oxidation curve contains three distinguishable regimes corresponding to different stages of oxide-scale evolution. These were fitted independently to evaluate the progression of diffusion control. The stage I (10–30 h) is rapid transient oxidation during which the oxidation rate (k_{p1}) is relatively high:

$$k_{p1} \approx 4.5 \times 10^{-2}\ \text{mg}^2\ \text{cm}^{-4}\ \text{h}^{-1} \quad (3)$$

This regime is dominated by the formation of transient TiO_2, Cr_2O_3, and NiO. Short-circuit diffusion along grain boundaries and dendritic interfaces. Competition among multiple reactive species before Al enrichment reaches the surface. The rapid early growth reflects mixed control, where both interface reaction and cation diffusion contribute to mass gain. The stage II (30–70 h) demonstrates steady protective parabolic growth (k_{p2}) in which the alloy enters a stable parabolic regime:

$$k_{p2} \approx 2.6 \times 10^{-2}\ \text{mg}^2\ \text{cm}^{-4}\ \text{h}^{-1} \quad (4)$$

This is the longest and most dominant stage. Microstructurally, this corresponds to the formation and thickening of a continuous Al_2O_3 layer, the development of an underlying SiO_2-rich sublayer, which significantly lowers oxygen diffusivity and the reduction of short-circuit pathways as transient oxides dissolve or are buried. At this stage, the oxidation mechanism transitions to classical diffusion control dominated by oxygen ingress through the protective alumina scale. While stage III (70–100 h) is highly protective, diffusion-limited regime being the final stage, the oxidation rate (k_{p3}) decreases further:

$$k_{p3} \approx 1.9 \times 10^{-2}\ \text{mg}^2\ \text{cm}^{-4}\ \text{h}^{-1} \quad (5)$$

This slowdown is associated with densification of the Al_2O_3 scale, possible transformation of metastable θ- Al_2O_3 into the slower-growing α- Al_2O_3, completion of the silica barrier, which acts as an "oxygen diffusion shut-off layer" and elimination of fast-diffusion pathways through scale healing. The oxide layer at this point is highly stable and markedly diffusion-limited, demonstrating excellent long-term oxidation resistance. Following the initial transient period, the kinetics undergo a discernible transition, and the rate of mass gain decreases. This marks the onset of a parabolic growth regime, signifying that diffusion through the oxide scale has become the rate-limiting step [27]. This transition is attributed to the formation of a continuous, internal layer of Al_2O_3 beneath the initial TiO_2-rich scale. The establishment of this alumina layer acts as a more effective diffusion barrier, slowing the inward diffusion of oxygen and the outward diffusion of metal cations.

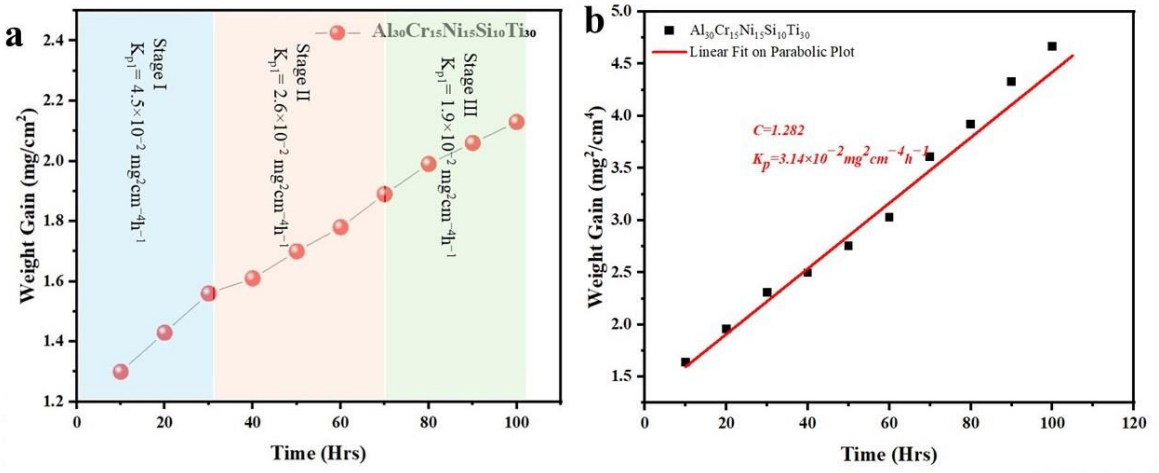

Figure 4: (a) Isothermal oxidation behaviour of $Al_{30}Cr_{15}Ni_{15}Si_{10}Ti_{30}$ at 1000 °C showing three kinetic regimes. Stage I (0–30 h) exhibits rapid initial oxidation ($k_{p1} = 4.5 \times 10^{-2}$ mg² cm⁻⁴ h⁻¹), followed by slower growth in Stage II (30–70 h, $k_{p2} = 2.6 \times 10^{-2}$ mg² cm⁻⁴ h⁻¹) and Stage III (70–100 h, $k_{p3} = 1.9 \times 10^{-2}$ mg² cm⁻⁴ h⁻¹), and (b) Parabolic fit of $(\Delta W)^2$ vs. time, yielding a global parabolic

rate constant $k_p = 3.14 \times 10^{-2}$ mg² cm⁻⁴ h⁻¹ and intercept $C = 1.282$, reflecting overall transient oxidation

However, the long-term kinetics show a gradual mass gain that is higher than what would be expected for a perfectly stable Al_2O_3 scale. This can be attributed to the continued instability of the outer scale. The porous TiO_2 layer offers limited protection and may experience micro-cracking due to thermal stresses, providing localized pathways for oxygen. The total weight gain after 100 hours was approximately 2.1 mg cm^{-2}, which is significantly higher than that of protective alumina-formers (typically <1 mg cm^{-2} after 100 h at 1000 °C) [28].

3.4 Morphology and Composition of the Oxide Scale

The surface morphology of the oxidised sample (Figure **5**) reveals a coarse, crystalline oxide structure with a porous, non-uniform appearance. The combined SEM-EDS and EPMA results conclusively demonstrate that the oxidation of the $Al_{30}Cr_{15}Ni_{15}Si_{10}Ti_{30}$ HEA proceeds through a complex, multi-stage process dominated by the competition between Ti and Al. The surface EDS analysis confirms that the initial oxidation front is dominated by titanium, resulting in a non-protective, porous matrix of TiO_2, with discrete nodules of a Ni-Cr spinel phase. This initial, fast-growing scale is inherently non-protective. However, the high activity of Al enables the subsequent formation of a continuous internal Al_2O_3 layer, as revealed by EPMA, which acts as the primary diffusion barrier beneath the Ti-rich outer scale, thereby moderating the oxidation rate from linear to parabolic. The inability to form a continuous, external Al_2O_3 scale is attributed to the excessive Ti content, which disrupts the selective oxidation process necessary for optimal protection by consuming the available oxygen at the gas/scale interface and forming a rapidly growing, non-adherent oxide. Furthermore, the extensive formation of subsurface phases underscores the microstructural instability of the alloy under high-temperature oxidising conditions.

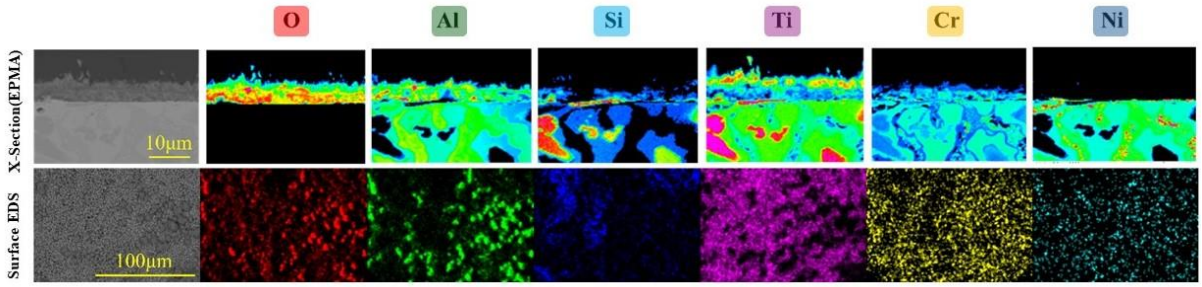

Figure 5: Cross-sectional EPMA and surface SEM-EDS elemental maps of the $Al_{30}Cr_{15}Ni_{15}Si_{10}Ti_{30}$ high-entropy alloy after isothermal oxidation at 1000 °C for 100 h. (Top): BSE image and EPMA maps (O, Al, Si, Ti, Cr, Ni) showing the oxide scale and subsurface region. (Bottom): Surface SEM-EDS (O, Al, Si, Ti, Cr, Ni) revealing lateral elemental distribution on the oxidized surface

The EPMA line-scan data along the 12.02 μm measurement marked in the oxygen mapping presented in

Figure **6**(a) and 6(b) provide detailed insight into the oxidation mechanism of the $Al_{30}Cr_{15}Ni_{15}Si_{10}Ti_{30}$ high-entropy alloy at 1000 °C. The data clearly reveal a non-protective, multilayered oxide scale structure dominated by outward Ti diffusion and inward oxygen penetration. As shown in

Figure **6**(a), the outermost region (0–3 μm) is characterised by high Ti and O intensities, confirming the formation of a porous TiO_2-rich external scale. This is accompanied by moderate Cr enrichment in the near-surface layer, indicative of a thin mixed $(Ni,Cr)_2O_3$ oxide. Beyond ~3 μm, oxygen intensity remains elevated while Ti decreases sharply, marking the transition into the secondary oxidation zone. A prominent Al peak appears between approximately 3.5 and 7 μm, corresponding to the precipitation of internal Al_2O_3 particles. Si also shows moderate enrichment in this region, consistent

with localised SiO_2 formation. In contrast, Ni and Cr intensities are marginally high within the scale and secondary oxidation zone.

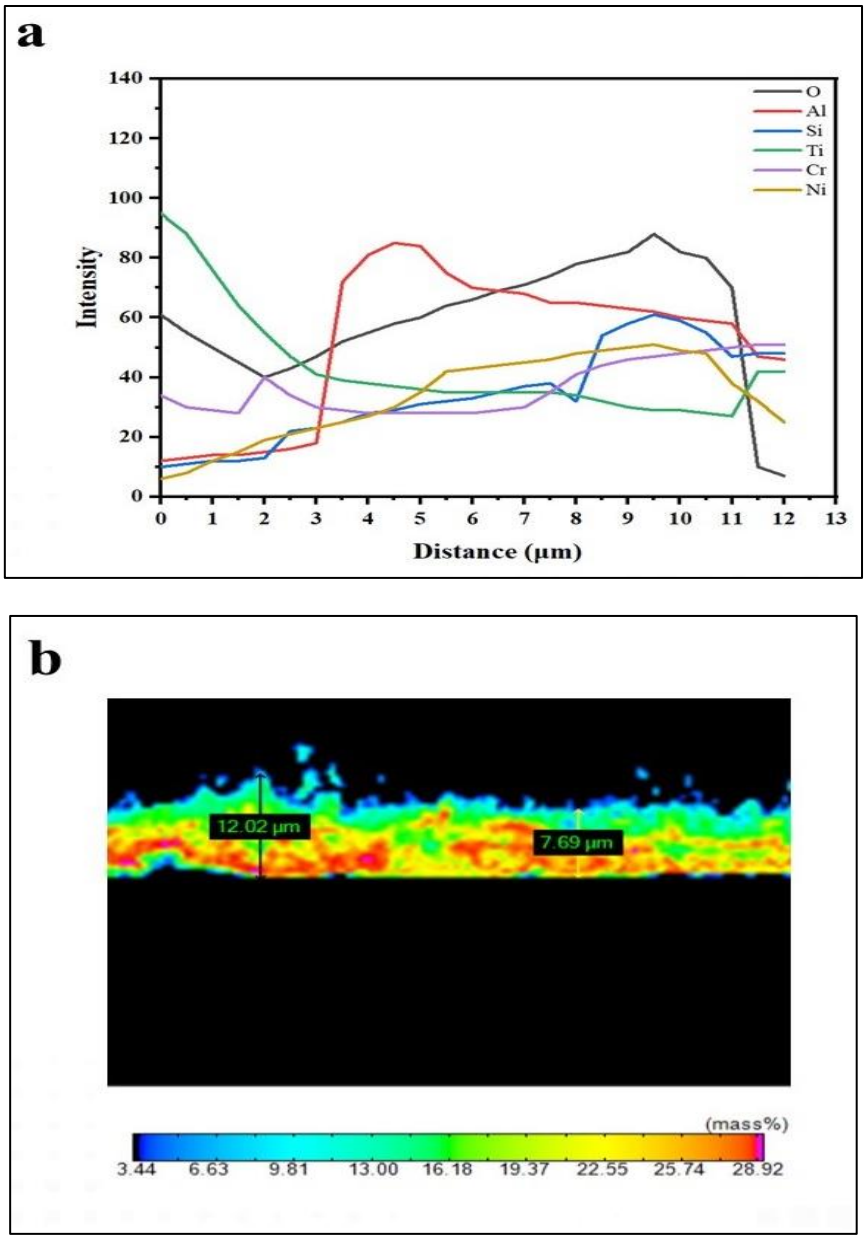

Figure 6: EPMA line scan and elemental map of the oxide scale formed on the $Al_{30}Cr_{15}Ni_{15}Si_{10}Ti_{30}$ high-entropy alloy after oxidation at 1000 °C for 100 h. (a) Line profiles showing intensity variation of O, Al, Si, Ti, Cr, and Ni across the scale and substrate as a function of distance from the outer surface, and (b) Corresponding EPMA color map with indicated thicknesses of the external oxide scale (12.02 µm)

The XPS surface analysis (Figure **7**) of the oxidized $Al_{30}Cr_{15}Ni_{15}Si_{10}Ti_{30}$ HEA reveals a complex mixture of oxides consistent with the multi-layered oxidation mechanism illustrated in the schematic. The survey spectra detect contributions from Al_2O_3, TiO_2, and $(NiCr)_2O_3$ simultaneously due to XPS probing only the top ~5–10 nm of the surface, reflecting the coexistence of a porous TiO_2 top layer, subsurface spinel, and internal alumina patches. High-resolution peak deconvolution shows Al 2p peaks at ~74.3 eV corresponding to Al^{3+} in Al_2O_3, Ti $2p_{3/2}$ peaks at ~458.5 eV assigned to Ti^{4+} in TiO_2, and Cr $2p_{3/2}$ and Ni $2p_{3/2}$ peaks at ~576 eV and ~855 eV, respectively, indicating spinel formation ($(NiCr)_2O_3$). The deconvolution further reveals minor contributions from lower oxidation states (Ti^{3+},

Cr^{3+}/Cr^{2+}), suggesting sub-stoichiometric or partially reduced oxide regions within the porous TiO_2 and spinel layers [29]. This multi-component oxide distribution confirms the selective outward diffusion of Al^{3+} and Ti^{4+}, the formation of protective alumina patches, and the accumulation of Cr/Ni spinels beneath the porous TiO_2, in agreement with the schematically proposed oxidation mechanism. The Al 2p and Si 2p spectra appear as single symmetric peaks because their spin-orbit splitting energies (≈0.4 eV for Al 2p and ≈0.6 eV for Si 2p) are smaller than the instrumental resolution, causing the $2p_{3/2}$ and $2p_{1/2}$ components to overlap completely. In contrast, Cr 2p, Ni 2p, and Ti 2p have much larger spin-orbit splitting (Cr 2p: ~9.2–9.8 eV; Ni 2p: ~17.3 eV; Ti 2p: ~5.7–6.1 eV). These separations are easily resolved, producing clear doublets ($2p_{3/2}$ and $2p_{1/2}$) that's why larger spin-orbit splitting and multiplet/satellite features in Cr 2p, Ni 2p, and Ti 2p result in well-resolved doublets and additional components.

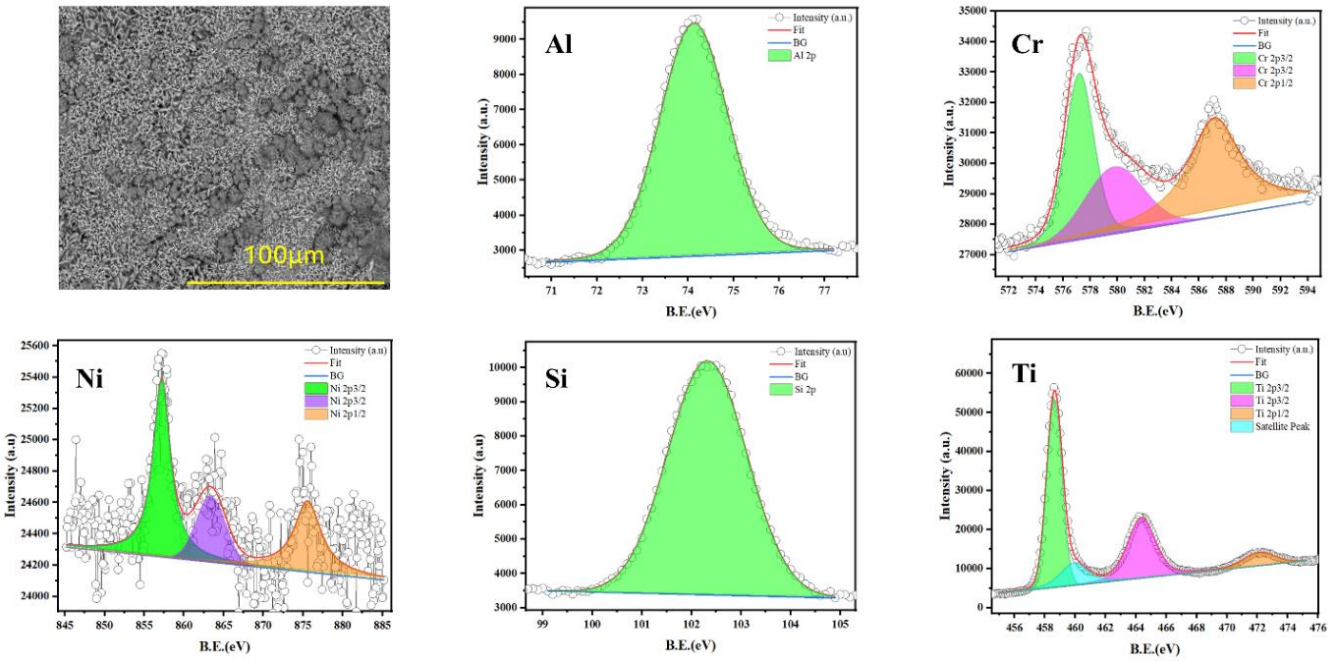

Figure 7: SEM surface morphology and high-resolution XPS core-level spectra (Al 2p, Cr 2p, Ni 2p, Si 2p, Ti 2p) of the oxide scale formed on the $Al_{30}Cr_{15}Ni_{15}Si_{10}Ti_{30}$ high-entropy alloy after oxidation at 1000 °C for 100 h. Peak fitting confirms the presence of Al^{3+}, Cr^{3+}, Ti^{4+}, Si^{4+}, and Ni^{2+} oxidation states

3.5 Deconstruction of the Oxidation Mechanism

Despite exceptional structural stability, the oxidation behaviour diverged significantly from conventional protective mechanisms. Oxidation of HEAs is governed by the competition between constituent oxides for oxygen affinity, diffusion rates, and thermodynamic stability [30]. At 1000 °C, TiO_2 formation dominated, leading to a porous, non-adherent oxide layer rather than a continuous Al_2O_3 or Cr_2O_3 scale typically desired for protection. In Al–Ti-containing HEAs, rapid outward diffusion of Ti cations through the oxide layer promotes the formation of TiO_2 which grows non-uniformly and cracks due to its high Pilling–Bedworth ratio (≈1.7–1.9) [31]. The present observations of a porous TiO_2 scale align with similar findings in AlFeCrCoNiTi [32], where excessive Ti activity suppressed the establishment of an alumina sublayer.

Titanium, occupying 30 at.%, exhibits high oxygen diffusivity and strong thermodynamic driving force for oxidation ($\Delta G° = -889$ kJ mol^{-1} at 1000 °C) compared with Al or Cr oxides [33]. Its dominance ensures rapid nucleation and growth of TiO_2, thereby blocking the slower-diffusion processes required for Al_2O_3 nucleation at the metal-oxide interface. Consequently, TiO_2 grows via

cation outward diffusion, while oxygen ingress continues through cracks and grain boundaries, resulting in a multi-layered, porous oxide with poor adherence. Although Al possesses a higher oxygen affinity than Cr or Ni, it failed to form a continuous external Al_2O_3 film. Instead, internal oxidation occurred beneath the TiO_2 layer. This behaviour can be explained by the limited surface Al activity (due to its solid solution with Ni and Cr) and rapid oxygen ingress through the defective TiO_2.

A similar phenomenon is demonstrated in AlCrFeNiTi HEAs, where Ti-rich oxides acted as oxygen pumps, allowing subsurface Al oxidation [34]. The resulting dispersed Al_2O_3 nodules observed via XPS and SEM in this study confirm such internal oxidation. The absence of a continuous Cr_2O_3 scale, despite 15 at.% Cr, can be attributed to competitive oxidation kinetics. Cr oxidation competes unfavourably with Ti because the latter reacts much faster with oxygen. Additionally, at high Ti activity, Ti preferentially segregates to the surface, effectively depleting Cr from the outer oxide layer. It is reported that in AlCrTi-based HEAs, Cr_2O_3 formation is kinetically suppressed when the Ti/Cr atomic ratio exceeds 1.5 — a condition met in this alloy (Ti/Cr = 2) [35,36]. This explains why Cr enrichment was observed only at deeper oxide interfaces, indicating delayed participation in oxidation. The role of Si in oxidation remains nuanced. Si tends to form amorphous SiO_2 internally rather than externally, which may locally hinder oxygen transport but does not generate a continuous barrier [37].

Therefore, the oxidation mechanism in $Al_{30}Cr_{15}Ni_{15}Si_{10}Ti_{30}$ HEA can be summarized as follows: TiO_2 forms first and grows outwardly, Al oxidizes internally, Cr remains mostly inactive due to competitive kinetics, and SiO_2 forms sporadically. This divergence from the typical Al_2O_3/Cr_2O_3 protective scale paradigm defines the alloy's oxidation limitation. The oxidation kinetics derived from the weight gain test exhibited a developing parabolic mass-gain trend, suggesting non-protective oxide growth at the initial stage; however, it became parabolic as the Al_2O_3 sublayer acted as a diffusion barrier to Ti cations and oxygen. Such early linearity arises when the oxide layer remains porous, allowing continuous oxygen ingress. The high TiO_2 content, with its poor adherence and cracking tendency, supports this interpretation. The porous, multi-layered structure observed under SEM directly correlates with the linear kinetics and the degradation of surface integrity.

In contrast, the bulk structural integrity of the alloy was preserved, an important distinction. While oxidation degraded the surface, no phase transformations or microstructural destabilization occurred in the substrate. This dual behavior reflects a decoupling between oxidation and phase-stability phenomena. The high-temperature oxidation of the $Al_{30}Cr_{15}Ni_{15}Si_{10}Ti_{30}$ high-entropy alloy at 1000 °C is characterized by the formation of a non-protective, multilayered oxide scale, as depicted in

Figure **8**(a). The external scale comprises porous TiO_2 as the dominant phase, intermixed with $(NiCr)_2O_3$ and discontinuous SiO_2 patches. Rapid outward Ti^{4+} diffusion through oxygen-deficient rutile and inward oxygen ingress result in accelerated scale growth and porosity development. Beneath the TiO_2 scale, discrete internal Al_2O_3 precipitates form initially and then spread to form a continuous intermediate layer, while the subsurface region contains AlNi, Ti_5Si_4, and $Cr_{2.2}Ti_{0.8}Si$ phases, reflecting elemental partitioning induced by selective oxidation.

Comparative phase-stability analysis (

Figure **8**(b)) reveals that the HEA maintains superior microstructural stability relative to conventional Ni-based superalloys up to 1000 °C, avoiding rapid phase dissolution. In conventional Ni-based super alloys, their oxidation rate increases above 900 °C due to sublimation of Cr_2O_3 and inability to form a continuous protective α-Al_2O_3 layer. While high Ti content in $Al_{30}Cr_{15}Ni_{15}Si_{10}Ti_{30}$ HEA promotes external TiO_2 growth, which overrides the beneficial effects of 30 at.% Al, 15 at.% Cr, and 10 at.% Si. Localized SiO_2 patches provide limited sealing but are insufficient to suppress overall kinetics. This behavior highlights the strong competition between Al and Ti during oxidation in the Al-Cr-Ni-Si-Ti system. While the HEA offers advantages in phase stability over Ni-superalloys, its oxidation resistance remains limited by Ti-rich scale porosity. Optimization through higher Al/Ti ratios, reactive-element additions is necessary to promote continuous alumina formation and enhance high-temperature performance for potential applications in turbines and heat exchangers.

The findings offer valuable guidance for future design of oxidation-resistant HEAs. First, the Al/Ti/Cr balance must be re-optimized. Reducing Ti content below 20 at.% could mitigate rapid TiO_2 growth, allowing Al and Cr to dominate oxidation kinetics and form continuous Al_2O_3 or Cr_2O_3 scales. An improvement is demonstrated in oxidation resistance of $Al_{30}Cr_{15}Ni_{15}Si_{10}Ti_{30}$ HEA by precisely tuning Ti below the threshold for TiO_2 dominance. Second, increasing Al and Cr concentrations would promote competitive formation of Al_2O_3/Cr_2O_3, which are thermodynamically more stable ($\Delta G° \approx -1000$ to -1100 kJ mol^{-1}) and slower-growing, yielding superior protection [38]. Concurrently, Ni addition can enhance scale adhesion by forming NiAl-type interfacial bonds, thereby suppressing spallation. Finally, Si management is crucial. Although Si can refine microstructures and improve strength, excessive Si (>5 at.%) tends to segregate, forming brittle silicides and discontinuous SiO_2 phases. Keeping Si below 5 at.% or pairing it with Mo or Nb may stabilise oxide chemistry [35].

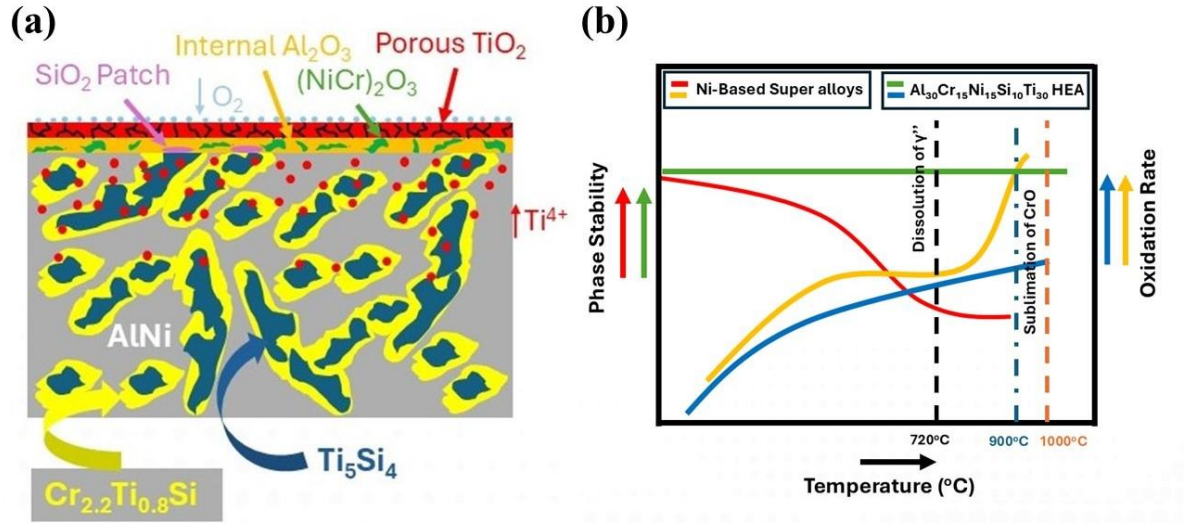

Figure 8: Schematic illustration of the high-temperature oxidation mechanism of the $Al_{30}Cr_{15}Ni_{15}Si_{10}Ti_{30}$ high-entropy alloy at 1000 °C. (a) Cross-sectional view showing the multilayer oxide scale consisting of SiO_2 patches, porous TiO_2, and $(NiCr)_2O_3$, with internal Al_2O_3 precipitates. The substrate microstructure includes AlNi, Ti_5Si_4, and $Cr_{2.2}Ti_{0.8}Si$ phases. Arrows indicate inward O_2 diffusion and outward Ti^{4+} transport, and (b) Comparison of phase stability and oxidation rate versus temperature for the $Al_{30}Cr_{15}Ni_{15}Si_{10}Ti_{30}$ HEA and conventional Ni-based superalloys, highlighting key transitions (γ′ dissolution, Cr_2O_3 sublimation) and divergent oxidation behavior above 900 °C

In conclusion, the high-temperature performance of the $Al_{30}Cr_{15}Ni_{15}Si_{10}Ti_{30}$ high-entropy alloy represents a paradigm shift in the property trade-offs inherent to conventional Ni-based superalloys (

Figure **8**(b)). While Ni-superalloys face an inescapable performance ceiling marked by the dissolution of the strengthening γ" phase and the sublimation of the protective CrO layer at temperatures approaching 1000 °C, the AlCrNiSiTi HEA system fundamentally circumvents these issues. Our results demonstrate that the high-entropy-stabilised microstructure exhibits exceptional resistance to phase dissociation, providing a robust mechanical framework. The oxidation pathway, although currently suboptimal due to Ti dominance, is rooted in the formation of solid alumina and silicate phases, thereby entirely avoiding the volatile mass-loss mechanism of chromia. Therefore, this alloy system shifts the high-temperature degradation challenge from structural and chemical instability (as in Ni-superalloys) to the kinetic optimisation of protective scale formation.

This work confirms that the strategic design of HEAs within this compositional space provides a viable pathway to overcome the fundamental limitations of traditional alloys, positioning them as next-generation candidates for extreme environments that require simultaneous phase stability and surface protection. The future challenge lies not in achieving stability, but in compositionally tuning the Al/Ti/Cr balance to steer the oxidation mechanism from a mixed, non-protective regime towards

the exclusive formation of a continuous, external Al_2O_3 scale. Further studies involving cyclic oxidation, TEM interface analysis, and thermodynamic modelling are required to fully assess long-term durability.

4. CONCLUSIONS

This integrated study on the phase stability and oxidation behaviour of the $Al_{30}Cr_{15}Ni_{15}Si_{10}Ti_{30}$ high-entropy alloy in comparison with the conventional Ni-based super alloys at 1000 °C yields critical insights for the design of next-generation high-temperature materials. The principal conclusions are:

- The $Al_{30}Cr_{15}Ni_{15}Si_{10}Ti_{30}$ high-entropy alloy shows no detectable transformation or decomposition below the solidus, indicating strong phase stability during thermal exposure under the given DSC conditions, with a sensitivity threshold of 1.24 μV/mW and a detection threshold of 0.02 mW/mg, both observed up to 1100 °C.
- Oxidation follows parabolic kinetics ($k_p = 3.14 \times 10^{-2}$ $mg^2cm^{-4}h^{-1}$) with three regimes representing transient oxidation, partial alumina formation, and long-term diffusion control.
- Oxidation produces a non-protective, multilayered scale dominated by porous TiO_2, with embedded $(Ni,Cr)_2O_3$ spinel and a discontinuous internal Al_2O_3 sublayer.
- Final mass gain (~2.1 mg cm^{-2} after 100 h) exceeds that of effective alumina-forming alloys, indicating incomplete surface protection.
- Overall, the alloy exhibits robust phase stability but suboptimal oxidation resistance; optimising Ti/Al/Cr contents and ratios is necessary to enable continuous external Al_2O_3 formation for high-temperature use.

In essence, this study successfully decouples the mechanisms of bulk stability from surface degradation, establishing that the primary challenge for this material class is not achieving thermal stability, but rather controlling the kinetic competition during oxidation to engineer a protective surface scale.

Acknowledgments

The authors gratefully acknowledge the financial support from Universiti Teknologi Malaysia under Grant No. UTM Fundamental Research (Q.J130000.3824.23H15), Shenzhen Municipal Basic Research Program Key Projects JCYJ20241202124215018, Shenzhen Higher Education Institutions Sustaining Support Program 20231120233925001, and Guangdong Basic and Applied Basic Research Foundation 2024A1515011022.

Author Contributions

All authors contributed toward data analysis, drafting and critically revising the paper and agree to be accountable for all aspects of the work.

Disclosure of Conflict of Interest

The authors have no disclosures to declare.

Compliance with Ethical Standards

The work is compliant with ethical standards.

References

[1] Chyrkin, A., Nowak, W. J., Gunduz, K. O., Fedorova, I., Sattari, M., Froitzheim, J. & Stiller, K. M. (2023). Intergranular oxidation of additively manufactured Ni-base alloy 625: The role of Si. *Corrosion Science*, 219, 111234.

[2] Ding, Z., Cao, B., Luan, J. & Jiao, Z. (2021). Synergistic effects of Al and Ti on the oxidation behaviour and mechanical properties of $L1_2$-strengthened FeCoCrNi high-entropy alloys. *Corrosion Science*, 184, 109365.

[3] Fan, Q., Chen, H., Zhang, S., Wu, Z., Hao, X., Wang, T. & Gao, W. (2024). Microstructure evolution and degradation process of AlCrTiSiN coatings with different Si contents at high temperatures. *Surface and Coatings Technology*, 494, 131505.

[4] Hu, M., Li, C., Zhou, S., Guo, Q., Ma, Z., Li, H., Xia, X. & Liu, Y. (2025). Cooperatively controlling γ′ phase and $M_{23}C_6$ of a polycrystalline Ni_3Al-based superalloy: Microstructure and creep resistance. *International Journal of Plasticity*, 187, 104291.

[5] Huang, Y., Zhang, R., Zhou, Z., Zhang, P., Yan, J., Yuan, Y. & Sun, X. (2023). Microstructure optimization for higher strength of a new Fe–Ni-based superalloy. *Materials Science and Engineering: A*, 865, 144632.

[6] Jian, P., Jian, L., Bing, H. & Xie, G. (2006). Oxidation kinetics and phase evolution of a Fe–16Cr alloy in simulated SOFC cathode atmosphere. *Journal of Power Sources*, 158(1), 354-360.

[7] Ju, J., Shen, Z., Li, J., Xiao, B., Zhou, Y., Li, Q., Xiao, W., Lo, Y., Zeng, X.,Wang, J. & Yang, T. (2023). Unraveling the origin of the excellent high-temperature oxidation resistance of an AlCrFeNiTi complex concentrated alloy. *Corrosion Science*, 217, 111116.

[8] Garg, M., Grewal, H. S., Sharma, R. K. & Arora, H. S. (2023). Improving the high temperature oxidation resistance of high entropy alloy by surface modification. *Corrosion Reviews*, 41(1), 39-56.

[9] Kawagishi, K., Yeh, A. C., Yokokawa, T., Kobayashi, T., Koizumi, Y. & Harada, H. (2012). Development of an Oxidation-Resistant High-Strength Sixth-Generation Single-Crystal Superalloy TMS-238. In *Superalloys 2012*, Ed. Huron, E. S., Reed, C. R., Hardy, M. C., Mills, M. J., Montero, R. E., Portella, P. D. & Telesman, J. (Wiley, New Jersey), pp. 189-195.

[10] Ke, L., Meng, L., Fang, S., Lin, C., Tan, M. & Qi, T. (2023). High-temperature oxidation behaviors of $AlCrTiSi_{0.2}$ high-entropy alloy doped with rare earth La and Y. *Crystals*, 13(8), 1169.

[11] Kumar, S., Sourav, A., Murty, B., Chelvane, A. & Thangaraju, S. (2022). Role of Al and Cr on cyclic oxidation behavior of $AlCoCrFeNi_2$ high entropy alloy. *Journal of Alloys and Compounds*, 919, 165820.

[12] Li, G., Ma, F., Liu, P., Qi, S., Li, W., Zhang, K. & Chen, X. (2023). Review of micro-arc oxidation of titanium alloys: Mechanism, properties and applications. J*ournal of Alloys and Compounds*, 948, 169773.

[13] Li, S. & Yamaguchi, T. (2022). High-temperature oxidation performance of laser-cladded amorphous TiNiSiCrCoAl high-entropy alloy coating on Ti-6Al-4V surface. *Surface and Coatings Technology*, 433, 128123.

[14] Li, Z., Chai, L., Qi, L., Wang, Y., Liu, Y., Yang, T. & Zhao, Y. (2023). Laser-cladded Al-Cr-Ti ternary alloy coatings on Ti-4Al-2V alloy: Specific microstructure and enhanced surface performance. *Surface and Coatings Technology*, 452, 129073.

[15] Cui, R., Tang, X., Gao, M., Zhang, H. & Gong, S. (2012). Thermodynamic analysis of interactions between Ti–Al alloys and oxide ceramics. *Transactions of Nonferrous Metals Society of China*, 22(4), 887-894.

[16] Nong, Z. S., Lei, Y. N. & Zhu, J. C. (2018). Wear and oxidation resistances of AlCrFeNiTi-based high entropy alloys. *Intermetallics*, 101, 144-151.

[17] Pei, X., Du, Y., Wang, H., Li, T., Hu, M., Wang, H. & Liu, W. (2023). Effects of Al/Si on the oxidation behavior of a $TiZrV_{0.5}Nb_{0.5}$ refractory high entropy alloy at 1000 ℃. *Corrosion Science*, 224, 111527.

[18] Peng, H., Hu, L., Huang, S., Zhang, Y., Yi, Y., Li, L. & Baker, I. (2023). Thermal stability of microstructure and their influences on mechanical properties of precipitation-hardened medium-entropy alloy $Ni_{43.4}Co_{25.3}Cr_{25.3}Al_3Ti_3$. *Materials Characterization*, 203, 113156.

[19] Schellert, S., Weber, M., Christ, H. J., Wiktor, C., Butz, B., Galetz, M. C. & Gorr, B. (2023). Formation of rutile $(Cr,Ta,Ti)O_2$ oxides during oxidation of refractory high entropy alloys in Ta-Mo-Cr-Ti-Al system. *Corrosion Science*, 211, 110885.

[20] Shi, J., Meng, F., Huang, G., Liu, F., Zhai, L., Chen, Y. & Wang, L. (2024). Improving the oxidation resistance by forming continuous Al_2O_3 protective layer in alumina-forming austenitic stainless steel. *Surface and Coatings Technology*, 493, 131279.

[21] Smialek, J. L. (2022). Invited review paper in commemoration of over 50 years of oxidation of metals: alumina scale adhesion mechanisms: a retrospective assessment. *Oxidation of Metals*, 97(1-2), 1-50.

[22] Sonar, T., Ivanov, M., Trofimov, E., Tingaev, A. & Suleymanova, I. (2024). An overview of microstructure, mechanical properties and processing of high entropy alloys and its future perspectives in aeroengine applications. *Materials Science for Energy Technologies*, 7, 35-60.

[23] Taylor, M., Ding, R., Mignanelli, P. & Hardy, M. (2022). Oxidation behaviour of a developmental nickel-based alloy and the role of minor elements. *Corrosion Science*, 196, 110002.

[24] Verma, V., Belcher, C. H., Apelian, D. & Lavernia, E. J. (2024). Diffusion in high entropy alloy systems–A review. *Progress in Materials Science*, 142, 101245.

[25] Veselkov, S., Samoilova, O., Shaburova, N. & Trofimov, E. (2021). High-temperature oxidation of high-entropic alloys: A review. *Materials*, 14(10), 2595.

[26] Wang, X., Mercier, D., Zanna, S., Seyeux, A., Perriere, L., Laurent-Brocq, M. & Marcus, P. (2023). XPS study of the thermal stability of passivated NiCrFeCoMo multi-principal element alloy surfaces. *Surface and Interface Analysis*, 55(6-7), 457-465.

[27] Wang, Z., Yan, Y., Wu, Y., Zhang, Y., Zhao, X., Su, Y. & Qiao, L. (2023). Recent research progress on the passivation and selective oxidation for the 3d-transition-metal and refractory multi-principal element alloys. *Npj Materials Degradation*, 7(1), 86.

[28] Yang, Y., Gao, Y., Liu, C., Dong, J. & Lou, L. (2025). Synergistic evolution of $MC/M_{23}C_6$ carbides in a polycrystalline Ni-based superalloy during long-term aging: Elemental diffusion and interaction mechanisms. *Materials Characterization*, 229, 115462.

[29] Yin, L., Ma, J., Yang, F., Nie, Y., Meng, L., Wang, Y. & Liang, W. (2025). Influence of precipitates on the initial oxidation behavior of GH4169 superalloy at 1000 °C. *Corrosion Communications*, 19, 138-148.

[30] Yu, S., Zhan, X., Liu, F., Guo, Y., Wang, Q., Li, Y. & Fan, X. (2022). 900 °C oxidation resistance of Ni-base superalloys alloyed with different refractory elements. *Journal of Alloys and Compounds*, 904 (100-101), 164071.

[31] Yurchenko, N., Panina, E., Moskovskikh, D., Kapustin, D., Zhilina, M., Shekhawat, L. & Zherebtsov, S. (2024). Strength and oxidation resistance of Laves phase-containing refractory Nb-Ti-Zr-Cr alloys: Effect of chemical complexity. *Scripta Materialia*, 243, 115978.

[32] Zhang, L., Yan, W., Shi, Q., Li, Y., Shan, Y. & Yang, K. (2020). Silicon enhances high temperature oxidation resistance of SIMP steel at 700 °C. *Corrosion Science*, 167, 108519.

[33] Zhang, Z., Ding, R., Guo, Q., Liu, C. & Liu, Y. (2025). Enhancing tensile and creep properties of Inconel 617 superalloy via regulating the synergistic evolution of $M_{23}C_6$ carbides and γ′ phases. *Materials Science and Engineering: A*, 919, 147523.

[34] Zhang, Z., Ding, R., Liu, C., Yu, L. & Liu, Y. (2023). The precipitates evolution with related element interaction and redistribution during long-term high-temperature aging of Alloy 617. *Materials Characterization*, 199, 112783.

[35] Zhang, Z., Guo, Q., Ding, R., Liu, C. & Liu, Y. (2025). Multi-stage evolution mechanism of precipitate phases at twin boundaries in Inconel 617 superalloy during long-term aging. *Materials Characterization*, 222, 114835.

[36] Zhao, G., Zang, X. & Qi, F. (2020). Effect of boron on isothermal oxidation behavior of a nickel-base superalloy with high Al and Ti contents. *Journal of Alloys and Compounds*, 846, 156490.

[37] Zhao, P. F., Hou, K. L., Wang, M., Ou, M. Q., Yang, Y. q. & Ma, Y. C. (2025). Effects of sub-solvus ageing on the tensile and creep properties of a new cast nickel-based superalloy. *Journal of Materials Science & Technology*, 212, 289-302.

[38] Zhong, L., Liu, Y., Wang, X., Ren, Q., Hu, R., Du, H. & Jin, P. (2025). Improving the mechanical properties of a novel nickel-based superalloy via the cubic secondary γ′ and the regulation of tertiary γ′. *Journal of Alloys and Compounds*, 1017, 179120.